


Cite this: *RSC Sustainability*, 2023, 1, 1989

# The heat-promoted metal–support interaction of a PtCu/SiO<sub>2</sub> carbon-free catalyst for the methanol oxidation and oxygen reduction reactions†

Quanqing Zhao,<sup>a</sup> Han Zhi,<sup>b</sup> Liu Yang<sup>a</sup> and Feng Xu<sup>ab</sup> 

Pt shows excellent catalytic activity and acid stability towards the methanol oxidation reaction (MOR) and oxygen reduction reaction (ORR), but suffers from deactivation due to the weak interaction with the carbon support and the oxidation of carbon under operation. To solve the problem, herein, silica nanospheres were used to load PtCu nanoparticles as the carbon-free catalyst for the MOR and ORR. It is found that the heat treatment is crucial to regulate the metal–support interaction and enhance the catalytic performance. The PtCu/SiO<sub>2</sub> catalyst after heat treatment exhibits a specific activity (SA) nearly 7 times the value of Pt/C toward the MOR, and much better durability. The MOR mass activity of heat-treated PtCu/SiO<sub>2</sub> is over twice the value of the untreated one. The electron transfer promoted by heat treatment leads to an upshift of the d-band center of Pt, resulting in the increase of the absorption rate of methanol and the intermediates.

Received 15th June 2023

Accepted 28th July 2023

DOI: 10.1039/d3su00193h

rsc.li/rscsus

## Sustainability spotlight

Direct methanol fuel cells (DMFCs) are widely accepted as one of the promising green energy resources to replace fossil fuels and are now on their way to commercialization. Pt/C is the commonly used catalyst in DMFCs. The carbon support leads to deactivation during long-term operation. Moreover, carbon is a product of the petrochemical industry. In this work, SiO<sub>2</sub> was studied as the non-carbon support to load PtCu alloy. The results showed better performance towards the methanol oxidation reaction and comparable activity towards the oxygen reduction reaction of the PtCu/SiO<sub>2</sub>. Hence, the activity and durability of the Pt-based catalyst were enhanced and the carbon consumption of DMFCs was further cut, promoting the sustainability of our world.

## Introduction

Platinum (Pt) shows excellent catalytic activity and acid stability towards the methanol oxidation reaction (MOR) and oxygen reduction reaction (ORR), and hence, is regarded as the state-of-the-art catalyst of direct methanol fuel cells (DMFCs).<sup>1</sup> Carbon, widely used as the support for the Pt catalyst, possesses high electronic conductivity and large specific surface area,<sup>2</sup> resulting in high catalytic activity of the Pt/C catalyst. But the catalytic activity of Pt/C decreases owing to the oxidation of the carbon support under the operating conditions such as high potential, frequent start–stop cycles, and strongly acidic environment, and the interaction between Pt and carbon will be undermined which causes Pt migration and aggregation.<sup>3</sup> To address these issues, many researchers have focused on developing alternative support materials which interact strongly with metal nanoparticles and remain stable under operation.<sup>4</sup>

Non-carbon support materials, such as titania, alumina, ceria, silica, and tungsten oxide, have received wide attentions recently.<sup>5</sup> Most of the oxide materials are inert in an acidic environment and exhibit fascinating advantages over carbon. For example, the surficial groups (such as –OH) on silica promote the MOR through reacting with intermediate species (such as CO\*), and reduce the impact of Pt poisoning.<sup>6</sup> However, most non-carbon materials exhibit low conductivity which decreases the catalytic activity compared to the carbon support, due to the inherent wide bandgap. In the last decade, it has been revealed that tuning the metal–support interaction (MSI) is effective in tailoring the electronic structure and hence the catalytic performance. MSI engineering includes downsizing the metals, tuning the defects/interface and morphology, and so on.<sup>7–9</sup> Fundamentally, the electron transfer involved in the MSI is crucial to the catalytic performance. During electron transfer, excess electrons tend to accumulate at the interface of the support and metal,<sup>10</sup> which significantly enhances the adsorption and reactions of adsorbates,<sup>11</sup> leading to improved activity and higher conductivity.<sup>12</sup> The electron transfer from the support to Pt results in a downshift of the Pt d-band center and consequently weakens the adsorption of methanol and

<sup>a</sup>College of Materials Science and Engineering, Fuzhou University, Fuzhou, 350108, China. E-mail: xufeng@fzu.edu.cn

<sup>b</sup>School of Advanced Manufacturing, Fuzhou University, Jinjiang, 362200, China

† Electronic supplementary information (ESI) available. See DOI: <https://doi.org/10.1039/d3su00193h>



intermediate species,<sup>13,14</sup> which promotes the catalytic activity and durability.<sup>15</sup>

Another urgent issue is the rarity and high cost of Pt, making the DMFCs expensive and hindering their commercialization.<sup>16</sup> Using non-noble metals (such as Co, Ni, Cu) to form Pt based alloys is an effective way to solve the issue, and improve electrocatalytic activity.<sup>17</sup> Lu<sup>18</sup> and co-workers found that Cu could change the binding energy of Pt due to the strong electronic interaction between Pt and Cu. Cu donates electrons and the electron density increases around Pt sites, resulting in weaker chemisorption of intermediates.

Herein, we present a PtCu alloy catalyst supported on silica nanospheres. SiO<sub>2</sub>, an oxide widely used in industries, was herein studied as a non-carbon support to promote the MSI and hence the activities toward the methanol oxidation and oxygen reduction reactions. Through thermal treatments, the MSI was engineered and the d-band center of Pt was tuned, leading to enhanced MOR performance.

## Results and discussion

Fig. 1A shows the X-ray diffraction (XRD) patterns of the synthesized Cu/SiO<sub>2</sub> before and after heat treatment. The Cu/SiO<sub>2</sub> before heat treatment exhibited diffraction peaks centered at 43.2°, 50.3°, and 73.8°, which were assigned to copper (JCPDS 04-0836). The Cu/SiO<sub>2</sub> after heat treatment (HC300) showed not only copper diffraction signals, but also peaks at 36.5°, 42.4°, and 61.5°, relating to Cu<sub>2</sub>O (JCPDS 05-0667). The appearance of Cu<sub>2</sub>O was because the copper became activated and was slowly oxidized in the air after heat treatment.<sup>19</sup> The peaks are steep with a narrow half-peak width and strong intensity, indicating a large average grain size, which is calculated to be about 50 nm using the Debye–Scherrer formula below:<sup>20,21</sup>

$$D = K\lambda/(\beta \cos \theta) \quad (1)$$

where  $\lambda = 0.15406$  nm (Cu K $\alpha$ ). No SiO<sub>2</sub> signals were observed on either of the two XRD patterns due to the amorphous structure.<sup>22</sup> The XRD patterns of PtCu/SiO<sub>2</sub>-40% and HC300-40% are exhibited in Fig. 1B and the patterns of all the as-prepared catalysts are exhibited in Fig. S1.† The signal intensity of amorphous SiO<sub>2</sub> in the range of 20–30° decreased from PtCu/SiO<sub>2</sub>-10% to PtCu/SiO<sub>2</sub>-40%, owing to its weight ratio decrease. Each sample exhibited diffraction signals at 41.2°, 47.7°, 69.8°, and 84.3°, which were between the typical signals



Fig. 1 (A) XRD patterns of Cu/SiO<sub>2</sub> and HC300; (B) XRD patterns of PtCu/SiO<sub>2</sub>-40% and HC300-40%; (C) FTIR spectra of SiO<sub>2</sub> spheres, PtCu/SiO<sub>2</sub>-40% and HC300-40%.

of Pt (JCPDS 04-0802) and Cu, indicating the successful formation of the PtCu alloy.

The Fourier transform infrared spectroscopy (FTIR) results of SiO<sub>2</sub> nanospheres, PtCu/SiO<sub>2</sub>-40%, and HC300-40% are exhibited in Fig. 1C. The peaks centered at 800 and 471 cm<sup>-1</sup> represent the symmetrical stretching vibration and bending vibration of Si–O. The peaks centered at 949 cm<sup>-1</sup> represent the Si–O stretching vibrations of Si–O–H, revealing the rich silanol groups (Si–OH) on the SiO<sub>2</sub> surface. The peaks at 1100 cm<sup>-1</sup> represent the anti-symmetric stretching vibration of Si–O–Si.<sup>23</sup> The peaks at 1633 cm<sup>-1</sup> represent the bending or deformation mode of molecularly coordinated water and the peaks at 3424 cm<sup>-1</sup> represent the stretching vibration of O–H that were part of the water molecule and Si–OH.<sup>24</sup> These peaks were also observed on the other as-prepared catalysts (Fig. S2†). The Pt, Cu, and SiO<sub>2</sub> contents were calculated based on the ICP analysis (Table S1†). The Pt, Cu, and SiO<sub>2</sub> contents of PtCu/SiO<sub>2</sub>-40% were 58, 13, and 29 wt% respectively. After heat treatment, HC300-40% showed higher SiO<sub>2</sub> content (43 wt%) and lower Pt and Cu contents (46.6 and 10.4 wt% respectively) than PtCu/SiO<sub>2</sub>-40%, but the Pt:Cu atomic ratio remained almost unchanged (about 1.46). PtCu/SiO<sub>2</sub>-30% showed higher Pt content but lower SiO<sub>2</sub> and Cu contents after heat treatment, and the Pt:Cu atomic ratio became larger (increasing from 0.81 to 1.36). The differences in the content changes on PtCu/SiO<sub>2</sub>-30% and PtCu/SiO<sub>2</sub>-40% before and after heat treatment demonstrated that the PtCu alloy of PtCu/SiO<sub>2</sub>-40% was more stable than that of PtCu/SiO<sub>2</sub>-30%.

The microstructures of the SiO<sub>2</sub> nanospheres, PtCu/SiO<sub>2</sub>-40% and HC300-40% were investigated using a scanning



Fig. 2 (A) SEM image of SiO<sub>2</sub> nanospheres; (B) TEM image of SiO<sub>2</sub> nanospheres; (C–G) TEM and EDS images of PtCu/SiO<sub>2</sub>-40%; (H) magnification of a specific region of (C); (I) High resolution image of PtCu/SiO<sub>2</sub>-40%, showing the magnification of a specific region of (H); (J) TEM image of HC300-40%; (K and L) high resolution images of HC300-40%.



electron microscope (SEM) and transmission electron microscope (TEM). The solid SiO<sub>2</sub> nanospheres were mainly around 100 nm in diameter (Fig. 2A and B). The TEM and EDS images of PtCu/SiO<sub>2</sub>-40% showed the metal nanoparticles intimately attached on SiO<sub>2</sub> nanospheres, thus the PtCu alloy interacted strongly with SiO<sub>2</sub> nanospheres (Fig. 2C–G). The metal nanoparticles were mainly 5 nm in diameter (Fig. 2H) and a metal lattice spacing of 0.22 nm was observed, relating to the PtCu (111) facet (Fig. 2I). After heat treatment, most of the PtCu alloy was still loaded on the SiO<sub>2</sub> surface and the morphology slightly changed probably because of the heat treatment (Fig. 2J). The measurements of the PtCu (111) crystal plane showed that the spacing of the HC300-40% crystal plane turned into 0.225 and 0.247 nm respectively and the average spacing showed a value of 0.23 nm (Fig. 2K and L), showing that after heat treatment the lattice spacing increased. The elemental mapping (Fig. S3†) of HC300-40% demonstrated the homogeneous dispersion of Pt and Cu elements, and the intimate contact of PtCu and SiO<sub>2</sub>.

X-ray photoelectron spectroscopy (XPS) was carried out to investigate the electronic structures of Si, Cu, and Pt. The Si 2p orbital of PtCu/SiO<sub>2</sub>-40% exhibited a peak at around 103.68 eV, and that of HC300-40% exhibited a peak at 103.48 eV (Fig. 3A). There was a negative B.E. shift of the Si 2p after heat treatment, suggesting an increased electron density of HC300-40%. The Cu 2p orbital of PtCu/SiO<sub>2</sub>-40% showed peaks at 931.88 and 951.68 eV, and that of HC300-40% showed peaks at 932.48 and 952.18 eV (Fig. 3B). The Cu 2p orbital of HC300-40% showed a noticeably positive B.E. shift, suggesting that heat treatment leads to a decreased electron density. The Pt 4f orbital of PtCu/SiO<sub>2</sub>-40% showed peaks at 71.38 and 74.58 eV, and that of HC300-40% showed peaks at 71.68 and 74.88 eV (Fig. 3C). There was also a positive shift in Pt 4f binding energy after heat treatment, suggesting a decreased electron density. The HC300-30% showed similar shifts of Pt 4f, Cu 2p and Si 2p orbitals after heat treatment compared to HC300-40% (Table S2†). The positive shifts of Pt 4f and Cu 2p and the negative shift of Si 2p revealed that even though Cu donated electrons to Pt, the electron density of Pt still decreased and the electrons transferred from PtCu to SiO<sub>2</sub>, which demonstrated a strong MSI.<sup>7</sup>

The MOR activity of PtCu/SiO<sub>2</sub>-10%, PtCu/SiO<sub>2</sub>-20%, PtCu/SiO<sub>2</sub>-30%, and PtCu/SiO<sub>2</sub>-40% is compared in Fig. S3.† As the Pt loading increases, the activity rises and the PtCu/SiO<sub>2</sub>-40% shows much higher activity than the others; therefore, the discussion hereafter focuses on PtCu/SiO<sub>2</sub>-40% and HC300-40%. The ECSA was calculated from CV curves (Fig. 4A) using a hydrogen adsorption theory by assuming a monolayer

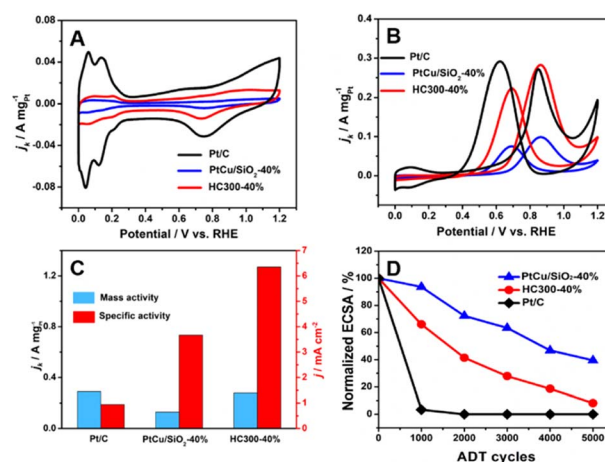


Fig. 4 (A) CVs of commercial Pt/C (20 wt% Pt), PtCu/SiO<sub>2</sub>-40%, and HC300-40%; (B) MOR activity; (C) mass and specific activities obtained from MOR results; (D) accelerating durability tests (ADT) of commercial Pt/C (20 wt% Pt), PtCu/SiO<sub>2</sub>-40%, and HC300-40%.

adsorption of hydrogen atoms on the surface of metallic catalysts ( $0.21 \text{ mC cm}^{-2}$ ).<sup>25</sup> The ECSA of Pt/C ( $30.8 \text{ m}^2 \text{ g}_{\text{Pt}}^{-1}$ ) was higher than that of PtCu/SiO<sub>2</sub>-40% ( $3.53 \text{ m}^2 \text{ g}_{\text{Pt}}^{-1}$ ) and HC300-40% ( $4.4 \text{ m}^2 \text{ g}_{\text{Pt}}^{-1}$ ) because the Pt nanoparticles of Pt/C exhibited smaller size (<5 nm) and better dispersion, and the electronic conductivity of the carbon support is higher.<sup>26</sup> The Nyquist plot illustrated that although the electronic resistance of SiO<sub>2</sub> nanospheres was higher than that of carbon, it was low enough as a support (Fig. S4†). The PtCu/SiO<sub>2</sub>-40% demonstrated even lower resistance than SiO<sub>2</sub>, and the resistance was further reduced after heat treatment, which evidenced the strong MSI.

Relative to Pt/C, PtCu/SiO<sub>2</sub>-40% showed poor MOR activity, but HC300-40% exhibited comparable activity (Fig. 4B). The mass activities (MAs) of HC300-40% ( $0.28 \text{ A mg}_{\text{Pt}}^{-1}$ ) and Pt/C ( $0.29 \text{ A mg}_{\text{Pt}}^{-1}$ ) were very close (Fig. 4C); the MA of PtCu/SiO<sub>2</sub>-40% was  $0.13 \text{ mg}_{\text{Pt}}^{-1}$ , less than half that of HC300-40%. The HC300-30% also showed an increase of MOR activity compared to PtCu/SiO<sub>2</sub>-30% (Table S3†).

The ratio of peak current densities of the forward scan ( $I_f$ ) to backward scan ( $I_b$ ) is commonly used to identify the poison resistance of the catalysts.<sup>27</sup> In the forward scan, methanol was oxidized into intermediates which strongly adsorb on the active sites, then in the backward scan the intermediates resume being oxidized.<sup>28</sup> Higher  $I_f : I_b$  ratios indicate that more intermediates are oxidized in the forward scan, leaving less to the backward scan. Compared to the  $I_f : I_b$  ratio of 0.93 (Pt/C), PtCu/SiO<sub>2</sub>-40% and HC300-40% demonstrate higher values of 1.30 and 1.27. Obviously, the poisoning resistance of the PtCu/SiO<sub>2</sub> catalysts is improved significantly. The specific activities (SAs) of PtCu/SiO<sub>2</sub>-40% and HC300-40% are  $3.66$  and  $6.35 \text{ mA cm}^{-2}$  respectively, and the SA of HC300-40% is nearly 7 times the value of Pt/C ( $0.95 \text{ mA cm}^{-2}$ ).

The durability of the catalyst is a highly important issue and was also tested (Fig. 4D). The ECSA of Pt/C decreased significantly in the first 1000 cycles, which meant poor durability due

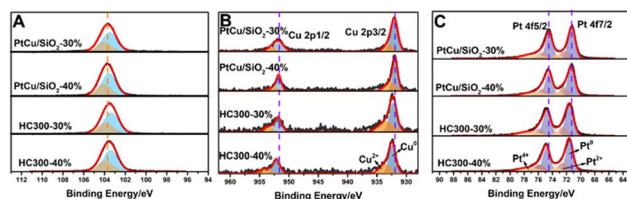


Fig. 3 XPS spectra of the Si 2p (A), Cu 2p (B), and Pt 4f (C) orbitals of PtCu/SiO<sub>2</sub>-30%, HC300-30%, PtCu/SiO<sub>2</sub>-40% and HC300-40%.



to the weak metal–support interaction and the oxidation of the carbon support.<sup>29</sup> The PtCu/SiO<sub>2</sub>-40% showed the best durability with 39.49% ECSA remaining after 5000 cycles, and an ECSA of 8.14% for HC300-40% remained after 5000 cycles. PtCu/SiO<sub>2</sub>-40% and HC300-40% retained 32.7% and 38% of their MOR activity and all catalysts retained more than 30% after 5000 cycles, and the *I<sub>f</sub>*:*I<sub>b</sub>* ratios of PtCu/SiO<sub>2</sub>-40% and HC300-40% were 1.26 and 1.24 respectively (Fig. S5†). Such slight decreases after ADT demonstrated the minor decline of poisoning resistance.

The analysis of electrochemical performance showed that the heat treatment was crucial to regulate the MSI between the SiO<sub>2</sub> and PtCu alloy and improve the MOR activity. The *I<sub>f</sub>*:*I<sub>b</sub>* ratios of PtCu/SiO<sub>2</sub>-40% and HC300-40% were 1.26 and 1.24 respectively (Fig. S4†). Such slight decreases after ADT demonstrated the minor decline of poisoning resistance. The electron transfer promoted by heat treatment led to an upshift of the d-band center of Pt,<sup>7</sup> which meant easier charge donation from Pt to the adsorbates and the chemisorption on Pt became stronger, leading to the increase of the absorption rate of methanol and the intermediates.<sup>30–32</sup> In the durability test, the ECSA of HC300-40% drops more than that of PtCu/SiO<sub>2</sub>-40%, owing to the increase of the absorption rate of the intermediates such as CO\*. Meanwhile, the HC300-40% showed less MOR activity decrease than PtCu/SiO<sub>2</sub>-40% after ADT, due to the MSI which promoted charge accumulation at the interface during electron transfer and increased the specific activity of Pt active sites, and the existing –OH at the interface protecting the Pt active sites from poisoning. Thus, the electron transfer caused by heat treatment led to much better MOR activity and the durability also improved.

Many studies have shown that the shift of the d-band center of Pt can change the ORR activity.<sup>21,33,34</sup> The ORR results (Fig. 5A) illustrated that PtCu/SiO<sub>2</sub>-40% and HC300-40% exhibited close onset potentials to Pt/C, but much better durability. After 10 000

cycles, the ORR activity of PtCu/SiO<sub>2</sub>-40% became better and that of HC300-40% remained unchanged, while that of Pt/C showed a significant decline (Fig. 5B–D). The PtCu nanoparticles strongly bonded to SiO<sub>2</sub> nanospheres due to the MSI, leading to improved ORR durability. The structural evolution of PtCu during the ORR was the reason for the better activity after ADT. Besides, the ascorbates were wiped out to form a clean surface during operation, leading to better activity.<sup>35</sup>

## Conclusions

SiO<sub>2</sub> nanosphere supported PtCu nanoparticles were successfully synthesized as carbon-free catalysts and exhibited much better activity and durability than Pt/C towards the methanol oxidation reaction. The as-prepared catalysts also showed comparable activity and better durability towards the oxygen reduction reaction. The heat treatment, which regulates the metal–support interaction, is crucial to the catalytic performance. The heat treatment promotes the electron transfer, which can adjust the d-band center of Pt. This work provides a strategy to synthesize a carbon-free catalyst with high MOR activity and durability, and reveals the importance of heat treatment for regulating the interaction between metal and non-carbon supports.

## Experimental

### The preparation of SiO<sub>2</sub> spheres

100 mL of ethanol and 10 mL of deionized water were mixed, then 3 mL of ammonium hydroxide was added to the ethanol stock and stirred for 10 minutes. Next, 1 mL of ethylsilicate was added drop by drop to the solution and stirred continuously for 24 h. Lastly, the solution was centrifuged at 12 000 rpm for 10 minutes to obtain the silica spheres. Then the SiO<sub>2</sub> spheres were washed three times with deionized water until pH = 7 and dried at 60 °C for 12 hours in the air.

### The preparation of Cu/SiO<sub>2</sub>

With magnetic stirring, 100 mL ethylene glycol, 200 mg of the as-prepared silica spheres and 1.5 g of copper nitrate trihydrate were added to a 250 mL three-neck flask. The copper nitrate was dissolved completely by stirring for 10 minutes, and then the silica spheres were dispersed by ultrasonication for 10 minutes. With constant bubbling of N<sub>2</sub> into the flask and stirring, the flask was refluxed at 210 °C in an oil bath for 30 minutes. Then it was kept stirring and cooled to room temperature. The solution was filtered and the obtained sample was washed three times with deionized water and lyophilized.

### The preparation of PtCu/SiO<sub>2</sub>

50 mg of the as-prepared Cu/SiO<sub>2</sub> and 35 mL of deionized water were dispersed by ultrasonication in a 50 mL flask. With magnetic stirring, 1.3 mL of chloroplatinate aqueous solution (4 mg mL<sup>-1</sup>) was added to the flask drop by drop. The solution was stirred at 60 °C for 6 h, and the obtained solution was filtered and washed three times. Then, the sample was mixed

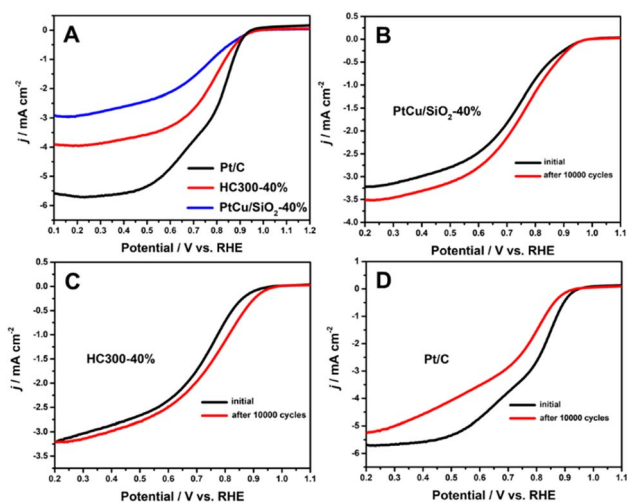


Fig. 5 (A) The ORR curves of Pt/C, HC300-40%, and PtCu/SiO<sub>2</sub>-40%; the changes in ORR polarization curves under potential cycling (scan rate 10 mV s<sup>-1</sup>, O<sub>2</sub> saturated) of PtCu/SiO<sub>2</sub>-40% (B), HC300-40% (C) and Pt/C (D).



with 30 mL of 1 M nitric acid solution and stirred slowly for 24 h to obtain the samples with 10 wt% Pt loading, which was labelled PtCu/SiO<sub>2</sub>-10%. The difference in the synthesis of samples with Pt loading of 20 wt%, 30 wt%, and 40 wt% was that the additive amount of chloroplatinate aqueous solution was changed to 2.7 mL, 4.6 mL and 7.3 mL and the obtained samples were labelled as PtCu/SiO<sub>2</sub>-20%, PtCu/SiO<sub>2</sub>-30%, and PtCu/SiO<sub>2</sub>-40%, respectively.

50 mg of Cu/SiO<sub>2</sub> was placed in a tube furnace and calcined at 300 °C for 2 hours in an atmosphere of 10 vol% H<sub>2</sub>/N<sub>2</sub>. The obtained sample was named HC300, loaded with 30 wt% and 40 wt% Pt and treated with nitric acid solution. Then the solution was filtered and the obtained samples were washed three times with water and lyophilized, and named HC300-30% and HC300-40% respectively.

### The preparation of Pt/C

50 mg Vulcan XC-72, 42 mL ethylene glycol and 8 mL of chloroplatinate aqueous solution (4 mg mL<sup>-1</sup>) were mixed in a 250 mL flask and dispersed by ultrasonication for 10 min. The solution was stirred at 130 °C for 3 h in an oil bath. After cooling, the Pt/C catalyst was filtered and washed in deionized water 3 times and lyophilized.

### Electrochemical measurements

The electrochemical activity of the MOR and accelerated durability test (ADT) were tested on a CHI 660E. The tests were carried out in a three-electrode cell at room temperature. A glassy carbon electrode (GCE) ( $\phi = 0.196 \text{ cm}^2$ ) was used as the working electrode, and Ag/AgCl and platinum wire were used as the reference and counter electrodes, respectively. Electrochemical activity and durability tests of the ORR were performed in a three-electrode cell on a PGSTAT302N (Autolab). The ORR test was carried out using a rotating ring disk electrode (RRDE,  $\phi = 0.196 \text{ cm}^2$ ) as the working electrode.

The GCE was finely polished to a mirror-like surface with an Al<sub>2</sub>O<sub>3</sub> slurry (<50 nm) before use. Catalyst ink was prepared by mixing 2 mg of catalyst, 0.5 mL of isopropanol, 0.5 mL of deionized water and 10  $\mu\text{L}$  of Nafion with ultrasonic dispersion. 10  $\mu\text{L}$  of ink was dropped on the working electrode and dried in the air. Cyclic voltammetry (CV) was performed in a nitrogen saturated 0.5 M H<sub>2</sub>SO<sub>4</sub> electrolyte in the potential range of 0–1.2 V vs. the reversible hydrogen electrode (RHE) at the scanning rate of 100 mV s<sup>-1</sup>. The MOR activity test was performed in a nitrogen saturated solution containing 0.5 M H<sub>2</sub>SO<sub>4</sub> and 1 M methanol, and the CV program was selected for the MOR activity test. The MOR ADT was performed in 0.5 M H<sub>2</sub>SO<sub>4</sub> electrolyte in the potential range of 0.6–1.2 V vs. RHE at the scanning rate of 50 mV s<sup>-1</sup>. Before the ADT and after every 1000 cycles, the MOR activity test was performed and recorded.

For the ORR tests, CV was performed in O<sub>2</sub> saturated 0.1 M HClO<sub>4</sub> aqueous solution in the potential range of 0–1.2 V vs. RHE at the scanning rate of 50 mV s<sup>-1</sup>. Linear scanning voltammetry (LSV) was performed in O<sub>2</sub> saturated 0.1 M HClO<sub>4</sub> aqueous solution in the potential range of 0–1.2 V at the scanning rate of 10 mV s<sup>-1</sup> with the rotating speed of 1600 rpm. The

ADT was completed by performing CV in N<sub>2</sub> saturated 0.1 M HClO<sub>4</sub> aqueous solution in the potential range of 0.6–1.2 V at the scanning rate of 100 mV s<sup>-1</sup> for 5000 cycles.

## Author contributions

Quanqing Zhao: conceptualization, methodology, validation, formal analysis, investigation, writing – original draft. Liu Yang: methodology, formal analysis. Feng Xu: formal analysis, resources, validation, writing – review & editing, funding acquisition.

## Conflicts of interest

The authors declare no competing financial interest.

## Acknowledgements

We are grateful for the financial support from the Natural Science Foundation of Fujian Province (no. 2022J01089).

## Notes and references

- 1 J. Zhao, H. Zeng and Z.-X. Lu, *ACS Appl. Nano Mater.*, 2022, **5**, 13594–13600.
- 2 R. Qu, S. Tang, J. Zhang and L. Wu, *ACS Sustainable Chem. Eng.*, 2018, **6**, 15560–15569.
- 3 S. Takao, O. Sekizawa, G. Samjeské, T. Kaneko, K. Higashi, Y. Yoshida, X. Zhao, T. Sakata, T. Yamamoto, T. Gunji, T. Uruga and Y. Iwasawa, *ACS Appl. Mater. Interfaces*, 2018, **10**, 27734–27744.
- 4 S. G. Dali, J. Q. Bermejo, M. T. Izquierdo, J. C. Gutierrez, A. Celzard and V. Fierro, *RSC Sustain.*, 2023, **1**, 1270–1277.
- 5 J. J. Ogada, A. K. Ipadeola, P. V. Mwangi, A. B. Haruna, F. Nichols, S. Chen, H. A. Miller, M. V. Pagliaro, F. Vizza, J. R. Varcoe, D. M. Meira, D. M. Wamwangi and K. I. Ozoemena, *ACS Catal.*, 2022, **12**, 7014–7029.
- 6 A. A. Melvin, V. S. Joshi, D. C. Poudyal, D. Khushalani and S. K. Haram, *ACS Appl. Mater. Interfaces*, 2015, **7**, 6590–6595.
- 7 T. W. van Deelen, C. Hernández Mejía and K. P. de Jong, *Nat. Catal.*, 2019, **2**, 955–970.
- 8 C.-C. Ting, C.-H. Chao, C. Y. Tsai, I. K. Cheng and F.-M. Pan, *Appl. Surf. Sci.*, 2017, **416**, 365–370.
- 9 Z. Wang, S.-M. Xu, L. Tan, G. Liu, T. Shen, C. Yu, H. Wang, Y. Tao, X. Cao, Y. Zhao and Y.-F. Song, *Appl. Catal., B*, 2020, **270**.
- 10 B. Zhang and Y. Qin, *ACS Catal.*, 2018, **8**, 10064–10081.
- 11 M. Farnesi Camellone, F. Negreiros Ribeiro, L. Szabová, Y. Tateyama and S. Fabris, *J. Am. Chem. Soc.*, 2016, **138**, 11560–11567.
- 12 N. K. Oh, J. Seo, S. Lee, H.-J. Kim, U. Kim, J. Lee, Y.-K. Han and H. Park, *Nat. Commun.*, 2021, **12**, 4606.
- 13 Z. Hou, L. Dai, J. Deng, G. Zhao, L. Jing, Y. Wang, X. Yu, R. Gao, X. Tian, H. Dai, D. Wang and Y. Liu, *Angew. Chem., Int. Ed.*, 2022, **61**, e202201655.



- 14 Z. Hou, L. Dai, J. Deng, G. Zhao, L. Jing, Y. Wang, X. Yu, R. Gao, X. Tian, H. Dai, D. Wang and Y. Liu, *Angew. Chem., Int. Ed.*, 2022, **61**, e202201655.
- 15 Z. X. Xia, X. L. Xu, X. M. Zhang, H. Q. Li, S. L. Wang and G. Q. Sun, *J. Mater. Chem. A*, 2020, **8**, 1113–1119.
- 16 X. Du, W. Cai, Q. Zhang, L. Yang and H. He, *ACS Appl. Nano Mater.*, 2021, **4**, 9729–9737.
- 17 L. Lu, S. Chen, S. Thota, X. Wang, Y. Wang, S. Zou, J. Fan and J. Zhao, *J. Phys. Chem. C*, 2017, **121**, 19796–19806.
- 18 L. Lu, S. Chen, S. Thota, X. Wang, Y. Wang, S. Zou, J. Fan and J. Zhao, *J. Phys. Chem. C*, 2017, **121**, 19796–19806.
- 19 S. J. Kim, Y. I. Kim, B. Lamichhane, Y.-H. Kim, Y. Lee, C. R. Cho, M. Cheon, J. C. Kim, H. Y. Jeong, T. Ha, J. Kim, Y. H. Lee, S.-G. Kim, Y.-M. Kim and S.-Y. Jeong, *Nature*, 2022, **603**, 434–438.
- 20 L. Zhuo, Z. Zhao, Z. Qin, Q. Chen, S. Liang, X. Yang and F. Wang, *Composites, Part B*, 2019, **161**, 336–343.
- 21 B. Liu, Q. Zhang, Y. Li, Y. Hao, U. Ali, L. Li, L. Zhang, C. Wang and Z. Su, *CCS Chem.*, 2023, **5**, 209–220.
- 22 F. R. Zhang, K. P. Jiang, G. S. Zhu, H. R. Xu, X. Y. Zhang, Y. Y. Zhao, Y. J. Zhang, Q. B. Wang, P. F. Pang and A. B. Yu, *Sustainable Energy Fuels*, 2023, **7**, 1245–1255.
- 23 G. Chen, Q. Hu, F. Schulz, W. J. Parak, L. Wang, X. Cui, K. Yang, Z. Luo, A. Zeng and Q. Fu, *ACS Appl. Nano Mater.*, 2021, **4**, 9060–9067.
- 24 Y. Takeuchi, S. Obata, K. Ohkura and Y. Nishina, *ACS Mater. Lett.*, 2022, **4**, 2590–2596.
- 25 R. Sharma, S. Gyergyek and S. M. Andersen, *Appl. Catal., B*, 2022, **311**, 121351.
- 26 Z. Xu, H. Zhang, H. Zhong, Q. Lu, Y. Wang and D. Su, *Appl. Catal., B*, 2012, **111–112**, 264–270.
- 27 L. Huang, X. Zhang, Q. Wang, Y. Han, Y. Fang and S. Dong, *J. Am. Chem. Soc.*, 2018, **140**, 1142–1147.
- 28 D. Paital, V. Thambi, M. S. Kutwal and S. Khatua, *ACS Appl. Nano Mater.*, 2022, **5**, 13286–13294.
- 29 L. Fan, J. Zhao, X. Luo and Z. Tu, *Int. J. Hydrogen Energy*, 2022, **47**, 5418–5428.
- 30 S. Joo, K. Kim, O. Kwon, J. Oh, H. J. Kim, L. Zhang, J. Zhou, J.-Q. Wang, H. Y. Jeong, J. W. Han and G. Kim, *Angew. Chem., Int. Ed.*, 2021, **60**, 15912–15919.
- 31 D. Wang, Z. Chen, Y. Wu, Y. C. Huang, L. Tao, J. Chen, C. L. Dong, C. V. Singh and S. Wang, *SmartMat*, 2022, **4**.
- 32 Y. Zhou, L. Yu, J. Chang, L. Feng and J. Zhang, *Green Energy Environ.*, 2022, DOI: [10.1016/j.gee.2022.08.007](https://doi.org/10.1016/j.gee.2022.08.007).
- 33 H. Ma, Z. Zheng, H. Zhao, C. Shen, H. Chen, H. Li, Z. Cao, Q. Kuang, H. Lin and Z. Xie, *J. Mater. Chem. A*, 2021, **9**, 23444–23450.
- 34 Y. Yang, B. He, H. Ma, S. Yang, Z. Ren, T. Qin, F. Lu, L. Ren, Y. Zhang, T. Wang, X. Liu and L. Chen, *Acta Phys.-Chim. Sin.*, 2022, **0**, 2201050.
- 35 L.-M. Luo, W. Zhan, R.-H. Zhang, D. Chen, Q.-Y. Hu, Y.-F. Guo and X.-W. Zhou, *J. Power Sources*, 2019, **412**, 142–152.

